Applied Magnetic Resonance (2022) 53:671–683
https://doi.org/10.1007/s00723-021-01379-2

Applied
Magnetic Resonance

ORIGINAL PAPER

# Sequential Electron Transfer in a BODIPY–Aluminum(III) Porphyrin–$C_{60}$ Triad Studied by Transient EPR Spectroscopy

**Art van der Est[1] · Stephen Malcolm[1] · Niloofar Zarrabi[2] · Christopher O. Obondi[3] · Francis D'Souza[3] · Prashanth K. Poddutoori[2]**

Received: 22 April 2021 / Revised: 17 June 2021 / Accepted: 22 June 2021 /
Published online: 14 July 2021


## Abstract

Spin polarized transient EPR spectra are reported for an aluminum(III) porphyrin ($AlPorF_3$) triad in which the electron donor bis-triphenylaminoborondipyrromethene ($BDP\text{-}TPA_2$) is attached covalently to one face of the porphyrin and an imidazole-appended $C_{60}$ is attached by coordination of the imidazole group to the Al(III) center on the opposite face. Excitation of the porphyrin results in two sequential electron transfer steps leading to charge separation between $BDP\text{-}TPA_2$ and $C_{60}$. The transient EPR spectra measured at room temperature in the organic solvent *o*-dichlorobenzene consist of two emission/absorption antiphase doublets assigned to $(BDP\text{-}TPA_2)^{\bullet+}$ and $C_{60}{}^{\bullet-}$ in the radical pair generated by the charge separation. The two antiphase doublets show opposite net polarization with net emission on $(BDP\text{-}TPA_2)^{\bullet+}$and net absorption on $C_{60}{}^{\bullet-}$. It is proposed that the net polarization develops as a result of singlet–triplet mixing during the lifetime of the initial radical pair generated by either electron transfer from $^1AlPorF_3$* to $C_{60}$ or hole transfer from $^1AlPorF_3$* to $BDP\text{-}TPA_2$. Simulations of the spectrum only reproduce the observed line shape if the influence of singlet–triplet mixing is included. However, because the singlet–triplet mixing that occurs in the two possible primary radical pairs is similar, determining the order of the electron transfer and hole transfer steps unambiguously is challenging. It is argued that the larger reorganization energy and electronic coupling expected for the hole transfer make it the more likely the first step.

✉ Art van der Est
avde@brocku.ca

✉ Prashanth K. Poddutoori
ppk@d.umn.edu

[1] Department of Chemistry, Brock University, 1812 Sir Isaac Brock Way, St. Catharines, ON L2S 3A1, Canada

[2] Department of Chemistry and Biochemistry, University of Minnesota Duluth, 1038 University Drive, Duluth, MN 55812, USA

[3] Department of Chemistry, University of North Texas, 1155 Union Circle, #305070, Denton, TX 76203-5017, USA

## 1 Introduction

Light-induced electron transfer is the central process of light energy conversion and storage in natural and artificial photosynthesis. The transfer of charge associated with the electron transfer generates an energy rich oxidant and reductant thereby storing the energy of the absorbed photon. In natural photosynthesis, a quantum yield of close to unity is achieved by stabilizing the initial charge separation with secondary electron transfer along a chain of acceptors [1]. As a result of the increased distance between the oxidized donor and reduced acceptor, the lifetime of the charge separation is increased from about $10^{-9}$ s in the initial charge-separated state to more than $10^{-3}$ s. This provides enough time to allow diffusion limited electron transfer steps involving soluble donors and acceptors to occur and effectively store the absorbed energy. The high quantum yield comes at the cost of the loss of a significant portion of the absorbed energy as heat. Mimicking this process in synthetic complexes has been an active area of research for many years [2–9]. These complexes generally consist of a chromophore or photosensitizer that is attached via covalent bridges to a series of electron acceptors and/or donors and the primary goal, is to achieve stabilized charge separation through sequential electron transfer steps. However, characterizing the pathway of the electron transfer and the lifetimes of the steps can be challenging. Generally, time-resolved optical methods are used and although they can provide a great deal of information, the optical signatures of the various states are often difficult to distinguish.

From a magnetic resonance perspective, these systems are of great interest because the electron transfer generates a series of sequential spin correlated radical pairs [10–16]. The correlation of the electron spins arises from the fact that before the light excitation they occupy the same orbital and must, therefore, obey the Pauli principle. If the quantum yield of the electron transfer is to be high, it must outcompete processes such as fluorescence and intersystem crossing that depopulate the lowest excited singlet state of the photosensitizer. Thus, the initial charge separation occurs on a time scale that is far shorter than that of the motion of electron spins and hence the correlation between the spins persists in the radical pair. The secondary electron transfer steps must outcompete charge recombination in the primary radical pair, which typically has a lifetime on the order of $10^{-9}$ to $10^{-7}$ s. This time regime is comparable to that of the precession of electron spins and hence, the electron spin dynamics and the electron transfer kinetics can become intertwined. Because of this, time-resolved EPR (TREPR) spectroscopy can also be used for exploring the details of electron transfer in natural and artificial photosynthetic systems [17–20].

Tetrapyrroles such as porphyrins and phthalocyanines are popular choices as photosensitizers in photosynthetic reaction center mimics because of their strong absorption in the visible region and moderate redox potentials that allow them to act as both donors and acceptors [2, 21–25]. Their properties can also be easily tuned by incorporating different metals into the center of the tetrapyrrole ring and/or adding electron withdrawing or donating groups on the periphery. In most

cases, the donor–acceptor dyads and triads are constructed by also attaching the electron donors and/or acceptors to the periphery of the ring. Over the past several years, we have explored the possibility of using the unique properties of the main group element porphyrins in which the donors and acceptors can be attached axially to the element in the center of the porphyrin [21, 26–30]. This arrangement has the advantage that groups attached to opposite faces of the porphyrin do not interact with each other and modifications of the porphyrin periphery to control its redox potential do not affect the structure of the electron transfer pathway.

Aluminum(III) porphyrins are particular well-suited for these types of complexes [21]. In addition to the four coordination bonds to the nitrogen atoms of the tetrapyrrole ring, the Al(III) center can form an axial covalent bond via oxygen and also readily forms coordination bonds to Lewis bases such as pyridine and imidazole. These two types of bonding allow donors and acceptors to be attached axially to the porphyrin on opposite faces of the ring.

Recently, we reported the synthesis and initial characterization of an aluminum(III) porphyrin triad in which bis-triphenylaminoborondipyrromethene (BDP-$TPA_2$) was attached covalently to one face of the porphyrin and $C_{60}$ was coordinated via an attached imidazole on the opposite face [31]. The redox potential of BDP-$TPA_2$ makes it a good electron donor while $C_{60}$ is a good electron acceptor. The structure of the complex $C_{60}$-Im→AlPor$F_3$-BDP-$TPA_2$ is shown in Fig. 1. Time-resolved optical spectroscopy suggested that excitation of the porphyrin leads to multistep electron transfer between BDP-$TPA_2$ and $C_{60}$. However, the order of the steps and the lifetime of the charge-separated states were difficult to determine precisely. Both of these quantities are accessible from TREPR experiments. The spin polarization pattern of a spin correlated radical pair (SCRP) that is part of a sequence of RPs depends on the singlet–triplet mixing that occurs in all precursor RPs. Thus, it is possible to draw conclusions about the pathway by which it was formed, provided that sufficient mixing occurs in the precursors.

The optical data for $C_{60}$-Im→AlPor$F_3$-BDP-$TPA_2$ suggested that the lifetime of the intermediate RP is on the order of a few ns. This is precisely the time region in which the TREPR spectra of subsequent RPs are most sensitive to the singlet–triplet mixing of the precursor RP. Here, we report TREPR spectra and simulations for $C_{60}$-Im→AlPor$F_3$-BDP-$TPA_2$ and will show that they show clear evidence of precursor singlet–triplet mixing confirming that sequential electron transfer does indeed occur in the complex. However, because the parameters that govern the singlet–triplet mixing in the two possible precursors states are similar, the effect of the mixing on the spin polarization pattern of the observed spectra is similar. Thus, the present study also illustrates the limitations of TREPR in definitively establishing the electron transfer pathway in complex multi-modular donor–acceptor systems. However, it provides information that can be used together with other spectroscopic data and computations to rationalize the electron transfer sequence.

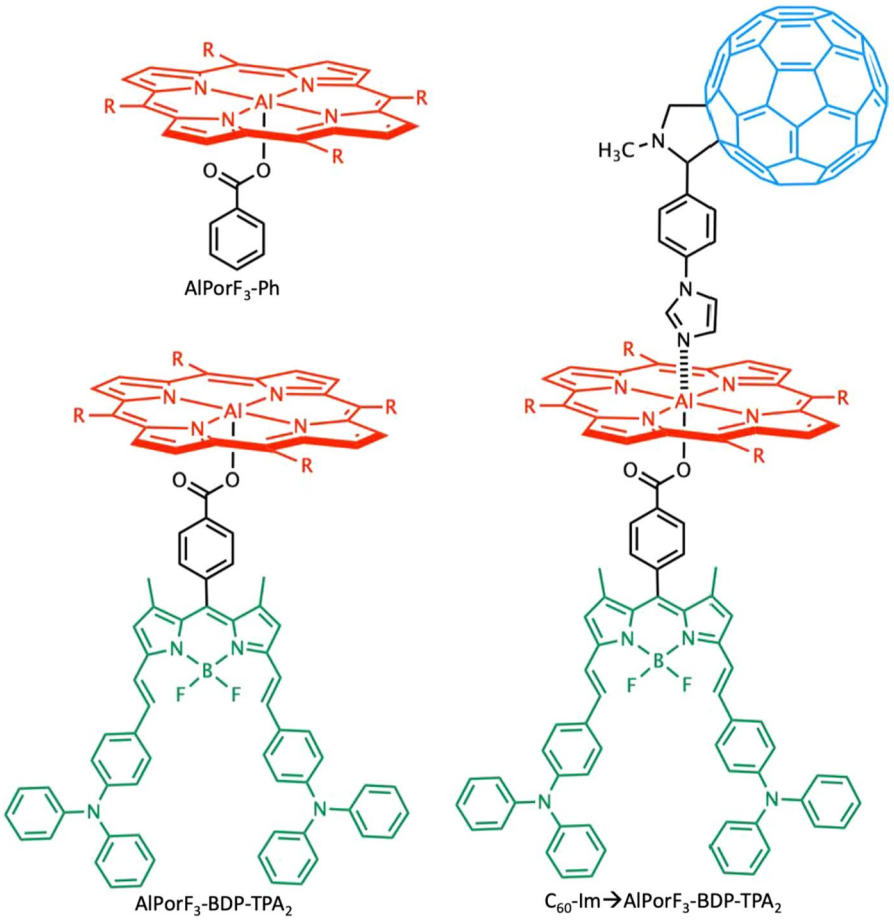


**Fig. 1** Chemical structures of the triad $C_{60}$-Im→$AlPorF_3$-BDP-$TPA_2$ ($R$ = 3,4,5-trifluorophenyl) and its reference compounds

## 2 Materials and Methods

### 2.1 Transient EPR Measurements

Transient EPR experiments were performed using a modified Bruker EPR 200D-SRC X-band spectrometer. Time/field datasets were collected at a microwave power of 6 mW. The EPR samples were prepared by dissolving the porphyrin complex in *o*-dichlorobenzene (*o*-DCB) or the liquid crystal 4-cyano-4'-pentylbiphenyl (5CB) to a concentration of ~ $7 \times 10^{-4}$ M. For the room temperature experiments on the *o*-DCB samples, the solution was placed in a flat cell and sealed with parafilm to prevent exposure to oxygen. The 5CB samples were placed in a 4-mm o.d. EPR tube and degassed by several freeze pump thaw cycles prior to

the measurements. The samples were excited at 532 nm using 10 ns pulses from a Surelite Nd:YAG laser at a repetition rate of 10 Hz and a pulse energy of 3 mJ.

### 2.2 DFT Calculations

The electronic structure of the triad $C_{60}$-Im→$AlPorF_3$-BDP-$TPA_2$ and the *g*-values of the radical ions were calculated using ORCA [32, 33] with the Perdew–Burke–Ernzerhoff (PBE) generalized gradient approximation density functional [34], the D3BJ dispersion correction [35] and the def2-TZVP basis set [36]. The resolution of identity approximation [37] with the def2/J auxiliary basis set was used to speed up the calculations. The structures of the components of the triad $TPA_2$-BDP, $AlPorF_3$ and $C_{60}$-Im were first constructed using the program Avogadro [38] and subjected to energy minimization using the UFF force field [39]. The geometries of the fragments were then optimized in ORCA. The triad was constructed from the geometry-optimized fragments and an optimization of the entire triad was carried out. The solvent was modeled using the Conductor-like Polarizable Continuum Model [40] with a dielectric constant of 9.93 and a refractive index of 1.5514 for *o*-DCB.

## 3 Results and Discussion

### 3.1 Formation and Electronic Structure of $C_{60}$-Im→$AlPorF_3$-BDP-$TPA_2$

As reported in ref. [31] the supramolecular triad, $C_{60}$-Im→$AlPorF_3$-BDP-$TPA_2$, can be constructed by titrating the dyad $AlPorF_3$-BDP-$TPA_2$ with $C_{60}$-Im. The observed shifts of the absorption and emission bands and isosbestic points are typical of coordination of Lewis bases to aluminum(III) porphyrins and show that the 1:1 self-assembled triad, $C_{60}$-Im→$AlPorF_3$-BDP-$TPA_2$ is formed. The UV−visible absorption spectrum of dyad $AlPorF_3$-BDP-$TPA_2$, also reported in [31], is essentially the sum of the spectra of the reference compounds $AlPorF_3$-Ph and BDP-$TPA_2$. Thus, the π- and π*-orbitals involved in the absorption transitions do not interact strongly with each other, and $AlPorF_3$ and BDP-$TPA_2$ can be treated as essentially independent species. This is confirmed by the frontier molecular orbitals of the triad determined by DFT calculations shown in Fig. 2. Consistent with the UV–visible absorption spectra, the orbital wave functions are localized on different parts of the molecule. As expected, the HOMO (Fig. 2a) is localized on the BDP-$TPA_2$ group and the LUMO (Fig. 2b) is on $C_{60}$. The HOMO–2 and LUMO+4 (Fig. 2c, d) are both localized on the porphyrin and represent the HOMO and LUMO of this part of the complex. Importantly, there is very little delocalization of the porphyrin orbitals onto the bridging groups that connect it to the fullerene and BDP-$TPA_2$.

### 3.2 Excited State Energies and Electron Transfer Pathways

The optical and electrochemical data reported previously [31] suggest that excitation of $AlPorF_3$ leads to two charge transfer reactions that result in charge

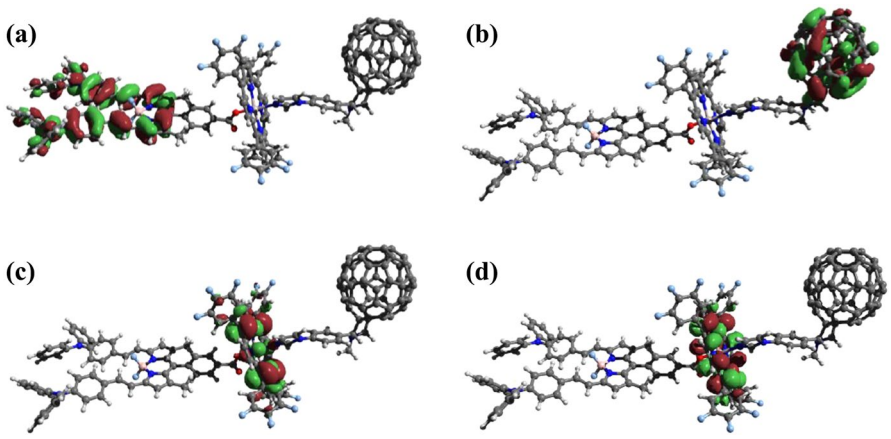


**Fig. 2** Frontier molecular orbitals of $C_{60}$-Im → $AlPorF_3$-BDP-$TPA_2$. **a** HOMO **b** LUMO **c** HOMO–2 (HOMO of AlPor) **d** LUMO + 4 (LUMO of AlPor). The green and red surfaces represent positive and negative electron density, respectively

separation between BDP-$TPA_2$ and $C_{60}$. Depending on the relative rates of the two reactions, there are two possible routes, route 1: $C_{60}$-Im → $^1$($AlPorF_3$)*-BDP-$TPA_2$ ⇒ $(C_{60})^{\bullet-}$-Im → $(AlPorF_3)^{\bullet+}$-BDP-$TPA_2$ ⇒ $(C_{60})^{\bullet-}$-Im → $AlPorF_3$-(BDP-$TPA_2$)$^{\bullet+}$ and route 2: $C_{60}$-Im → $^1$($AlPorF_3$)*-BDP-$TPA_2$ ⇒ $C_{60}$-Im → $(AlPorF_3)^{\bullet-}$-(BDP-$TPA_2$)$^{\bullet+}$ ⇒ $(C_{60})^{\bullet-}$-Im → $AlPorF_3$-(BDP-$TPA_2$)$^{\bullet+}$. Which of these two possibilities occurs is not certain, but the rate constants obtained from the transient absorbance data indicate that the charge separation between $TPA_2$-BDP and $AlPorF_3$ in the triad is about an order magnitude faster than the charge separation between $AlPorF_3$ and $C_{60}$. The lifetime of the final charge-separated state in the triad could not be determined accurately from the transient absorbance data but was estimated to be on the order of ~ 20 ns [31].

Figure 3 shows difference density plots of the charge transfer (CT) states obtained from time-dependent DFT calculations. The calculated energies, which also include the solvent stabilization in *o*-DCB predict that $(C_{60})^{\bullet-}$-Im → $AlPorF_3$-(BDP-$TPA_2$)$^{\bullet+}$ is the lowest energy excited state (Fig. 3a) and $C_{60}$-Im → $(AlPorF_3)^{\bullet-}$-(BDP-$TPA_2$)$^{\bullet+}$ (Fig. 3c) is the highest energy CT state. The solvent correction of ~ 1 eV appears to be overestimated in these calculations since it gives energies for the states shown in Fig. 3a and b that are lower than the ground state energy. However, the correction is roughly the same for all three states so that their relative energies do not depend strongly on the solvent.

### 3.3 TREPR Spectroscopy

To investigate whether TREPR data can be used to resolve the ambiguity in the order of the electron transfer steps and the lifetime of the final radical pair state, room temperature time/field datasets were collected in *o*-DCB and in the liquid crystal 5CB. Figure 4 shows a comparison of the TREPR

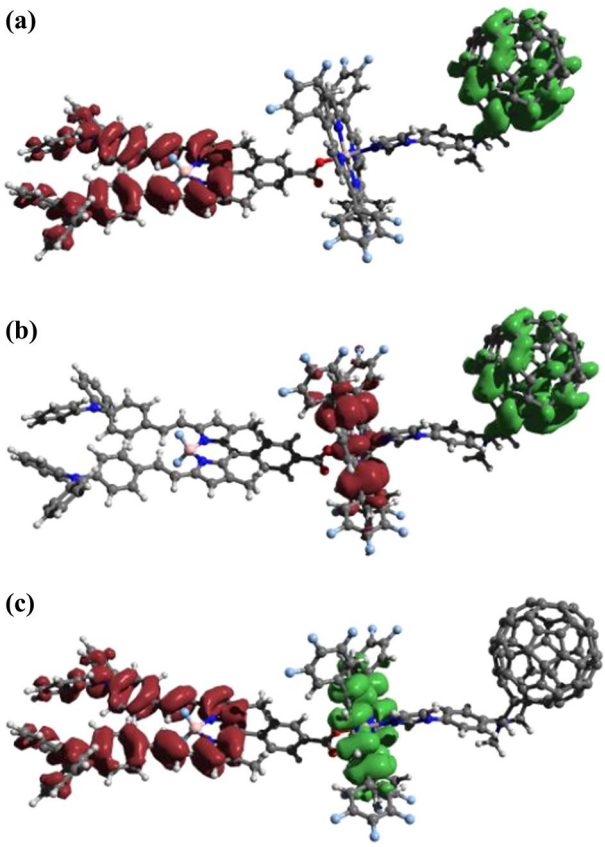


**Fig. 3** Difference densities of the charge transfer states of $C_{60}$-Im → $AlPorF_3$-BDP-$TPA_2$ from time-dependent DFT computations. **a** Lowest energy CT state $E = -1.152$ eV relative to the ground sate. **b** AlPor to $C_{60}$ charge transfer state, $E = -0.337$ eV. **c** BDT-$TPA_2$ to AlPor charge transfer state, $E = 0.119$ eV. The green and red surfaces represent positive and negative changes in electron density between the ground and excited state, respectively

spectra of $C_{60}$-Im → $AlPorF_3$-BDP-$TPA_2$ and the reference compound $C_{60}$-Im at 150 ns after the laser flash in the two solvents. Spectrum (a), which is $C_{60}$-Im → $AlPorF_3$-BDP-$TPA_2$ in *o*-DCB, arises primarily from the charge-separated state $(C_{60})^{\bullet-}$-Im → $AlPorF_3$-$(BDP\text{-}TPA_2)^{\bullet+}$ and consists of two overlapping emission/absorption (E/A) antiphase doublets with different linewidths. As can be seen in Table 1, the isotropic *g*-value of $(C_{60})^{\bullet-}$ obtained from DFT calculations is smaller than that of $(BDP\text{-}TPA_2)^{\bullet+}$. In addition, the inhomogeneous linewidth for $(C_{60})^{\bullet-}$ is expected to be smaller than that of $(BDP\text{-}TPA_2)^{\bullet+}$ because $(C_{60})^{\bullet-}$ does not contain any magnetic nuclei. Thus, we assign the narrow E/A doublet, which occurs at slightly higher field (smaller *g*-value), to $(C_{60})^{\bullet-}$ and the broader E/A pattern to $(BDP\text{-}TPA_2)^{\bullet+}$. The doublet from $(C_{60})^{\bullet-}$ appears to show net absorptive polarization while that from $(BDP\text{-}TPA_2)^{\bullet+}$ has net emission.

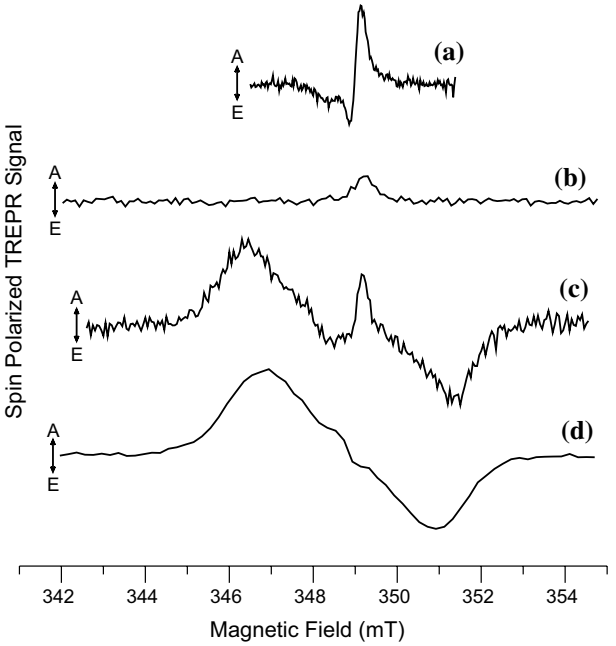


**Fig. 4** Room temperature TREPR spectra of the triad $C_{60}$-Im→$AlPorF_3$-BDP-$TPA_2$ and the reference compound $C_{60}$-Im in two different solvents. **a** $C_{60}$-Im→$AlPorF_3$-BDP-$TPA_2$ in *o*-DCB; **b** $C_{60}$-Im in *o*-DCB **c** $C_{60}$-Im→$AlPorF_3$-BDP-$TPA_2$ in the liquid crystal 5CB; **d** $C_{60}$-Im in 5CB. The spectra were extracted from the time-field dataset in a time window centered at 150 ns after the laser flash

**Table 1** The *g*-values of the radical ion species in the possible light-induced charge transfer states obtained from DFT calculations and other parameters used for the simulation of the spectra in Fig. 6

| | $(BDP\text{-}TPA_2)^{\bullet+}$ | $(AlPorF_3)^{\bullet+}$ | $(AlPorF_3)^{\bullet-}$ | $(C_{60})^{\bullet-}$ |
|---|---|---|---|---|
| *g*-values | 2.00284 | 2.00348 | 2.00119 | 2.00111 |
| Linewidths (mT) | 0.38 | 0.20 | 0.20 | 0.14 |
| | $(BDP\text{-}TPA_2)^{\bullet+}$-$(C_{60})^{\bullet-}$ | $(AlPorF_3)^{\bullet+}$-$(C_{60})^{\bullet-}$ | | $(BDP\text{-}TPA_2)^{\bullet+}$-$(AlPorF_3)^{\bullet-}$ |
| *J* (mT) | 0.08 | 1.5 | | 1.5 |
| Lifetime (ns) | 90 | 2.5 | | 2.0 |

Spectrum (b) is the triplet state of $C_{60}$ in *o*-DCB. The rapid isotropic motion leads to averaging of the zero-field splitting and cancelation of the multiplet polarization of the triplet state so that only a very weak absorptive signal is seen. In contrast, in the liquid crystalline solvent 5CB, in which the motion is anisotropic, the zero-field splitting is not averaged to zero and a prominent A/E pattern about 4 mT wide from the $C_{60}$ triplet state is seen for both the triad (spectrum (c)) and the

fullerene reference compound (spectrum (d)). The narrow features at the center of spectrum (c) arise from the charge-separated state and are similar to spectrum (a).

Figure 5 shows fits of the time traces taken at the absorptive and emissive maxima of the radical pair spectrum of $C_{60}$-Im→$AlPorF_3$-BDP-$TPA_2$ in *o*-DCB (spectrum (a) in Fig. 5). The time traces are fitted as the sum of two exponentially decaying components:

$$S(t, B_0) = \alpha(B_0)\exp(-k_{RP}t) + \beta(B_0)\exp(-k_{C_{60}}t), \tag{1}$$

where $\alpha(B_0)$ and $\beta(B_0)$ are the amplitudes of the signals from the radical pair $(C_{60})^{\bullet-}$-Im→$AlPorF_3$-(BDP-$TPA_2)^{\bullet+}$ and the fullerene triplet state, respectively, at a given field position, $B_0$. The decay rates of the two signals are governed by spin relaxation and decay to the ground state such that $k = {}^{1}/_{\tau_{rel}} + {}^{1}/_{\tau_{decay}}$. The lifetime of the $C_{60}$ triplet state is known to be ~ 50 µs at room temperature [41] and is negligible relative to the spin relaxation decay. For the radical pair, the spin relaxation lifetime is unknown, but it is clear from the time traces that the signal decay is much faster than that of the weak $C_{60}$ triplet state component. Radical pairs usually have longer spin relaxation times than triplet states, due to the weaker spin–spin coupling. Thus, decay of the radical pair TREPR signals appear to be dominated by charge recombination. In the fits, we have taken the observed relaxation lifetime for the $C_{60}$

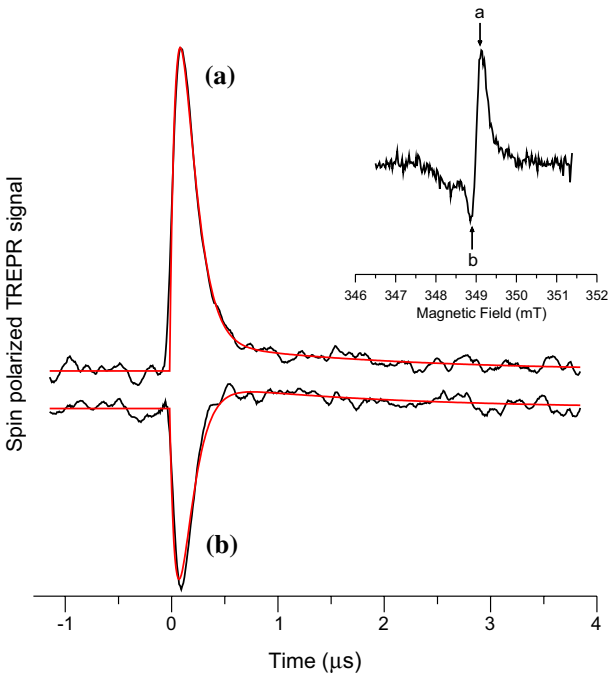


**Fig. 5** Kinetic fit of the spin polarized EPR transients from the triad $C_{60}$-Im→$AlPorF_3$-BDP-$TPA_2$ in *o*-DCB at room temperature. The transients were taken at **a** 349.1 mT and **b** 348.7 mT at the absorptive and emissive maximum of the spectrum as shown in the inset

triplet as a lower limit of $\tau_{rel}$ for the radical pair. Since this lower limit for $\tau_{rel}$ is much longer than the lifetime of the radical pair TREPR signal it has little effect on the fitted lifetimes. The ~ 100 ns rise time of the spectrometer is taken into account by convoluting $S(t)$ with an exponential response function:

$$S_{obs}(t) = \frac{\int_{-\infty}^{t} S(t') \exp(-(t-t')/\tau_{rise}) dt'}{\int_{-\infty}^{t} \exp(-(t-t')/\tau_{rise})}. \quad (2)$$

The fits of the transients yield a spin relaxation lifetime of 1.80 µs and a lifetime for the radical pair of 90 ns. The lifetime of the radical pair is somewhat longer than the value of ~ 20 ns obtained from optical data probably because the lifetime is close to the lower limit of the time resolution of the TREPR spectrometer and beyond the 3 ns time window of the optical pump-probe experiments reported in reference [31].

### 3.4 TREPR Spectral Simulations

For the triad, it is clear from the TREPR spectrum in 5CB that in addition to the charge-separated state, the triplet state of $C_{60}$ is also formed. However, in *o*-DCB, the motion is clearly fast enough to average the ZFS. Thus, we can safely assume that the weak dipolar coupling and any *g*-anisotropy in the radical pair will be averaged. We can also expect that the exchange coupling is smaller than the inhomogeneous linewidth. Under these conditions the line shape of the antiphase doublet is given by [17, 42, 43]

$$I_i = \frac{2J}{\sqrt{2\pi}\Delta\omega_i^3}(\omega_i - \omega_0) \exp\left(-\frac{(\omega_i - \omega_0)^2}{2\Delta\omega_i^2}\right), \quad (3)$$

where $i$ refers to the two radicals, $\omega_i = \hbar^{-1} g_i \beta B_0$ is the resonance frequency of each radical, $\Delta\omega_i$ is the inhomogeneous linewidth and $J$ is the isotropic exchange coupling the radical pair.

The fact that the each of the antiphase doublets in the experimental spectrum in *o*-DCB shows net polarization of opposite sign is indicative of singlet–triplet mixing in the initial radical pair state. The mixing results in two additional contributions to the polarization of subsequent radical pairs [17, 42, 43]. The singlet–triplet mixing that arises from the difference in the *g*-values of the radicals in the precursor radical pair leads to equal and opposite net polarization of each radical with intensity given by

$$I^z \propto \frac{\beta B_0}{h} \frac{2J_1(g_D - g_A)_1}{k^2}, \quad (4)$$

where $k$ is the decay rate, $J_1$ is the exchange coupling and $g_D$ and $g_A$ are the *g*-values of the donor and acceptor in the precursor radical pair. The inhomogeneous line broadening also contributes to the singlet–triplet mixing and leads to a multiplet contribution to the antiphase doublet of the radical that is not transferred:where Δω

is the inhomogeneous linewidth of the radical that is not directly involved in the secondary electron transfer step.

In $C_{60}$-Im → $AlPorF_3$-BDP-$TPA_2$, the initial radical pair can be either $(AlPorF_3)^{\bullet+}$-$(C_{60})^{\bullet-}$ or $(BDP\text{-}TPA_2)^{\bullet+}$-$(AlPorF_3)^{\bullet-}$. Thus, we have simulated the spectra in *o*-DCB assuming both scenarios. The simulated spectra have been calculated using the *g*-values obtained from DFT computations (Table 1). The exchange coupling and radical decay rates are unknown for the two possible initial radical pairs and these two parameters are interdependent in determining the spectrum of the second radical pair. Therefore, we have arbitrarily set the exchange coupling in the initial radical pair to $J_1 = 1.5$ mT and adjusted the lifetime to achieve best agreement with the experimental spectrum. The simulations are shown in Fig. 6.

The simulations in Fig. 6 show that the experimental polarization pattern is consistent with singlet electron transfer and a positive value for the spin–spin coupling in the radical pair $(BDP\text{-}TPA_2)^{\bullet+}$-$(C_{60})^{\bullet-}$. Since the spin–spin coupling is much smaller than the inhomogeneous linewidth, its value cannot be determined accurately from the spectrum. Thus, the value of *J* used in the simulations is just a reasonable estimate based on a survey of literature values from CIDNP data [44, 45]. In simulation (a) in Fig. 6, the initial charge separation is assumed to be electron transfer from $AlPorF_3$ to $C_{60}$, while in simulation (b) hole transfer from BDP-$TPA_2$ to $AlPorF_3$ is the first step. The simulations also include a weak contribution from

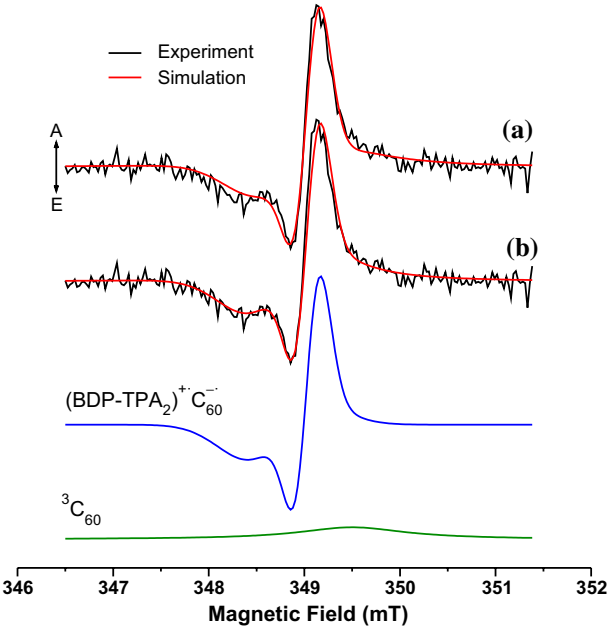


**Fig. 6** Transient EPR spectrum of $C_{60}$-Im → $AlPorF_3$-BDP-$TPA_2$ at room temperature in *o*-DCB using the parameters given in Table 1. **a** Comparison of the experimental spectrum (black) and simulated spectrum (red) assuming that $(AlPorF_3)^{\bullet+}$-$(C_{60})^{\bullet-}$ is the precursor to $(BDP\text{-}TPA_2)^{\bullet+}$-$(C_{60})^{\bullet-}$. **b** Simulation assuming that $(BDP\text{-}TPA_2)^{\bullet+}$-$(AlPorF_3)^{\bullet-}$ is the precursor. The contributions from $(BDP\text{-}TPA_2)^{\bullet+}$-$(C_{60})^{\bullet-}$ (blue) and the triplet state of $C_{60}$ (green) to simulation (b) are also shown

$^3(C_{60})$. The simulated $(BDP\text{-}TPA_2)^{\bullet+}\text{-}(C_{60})^{\bullet-}$ and $^3(C_{60})$ spectra used in simulation (b) are also shown in Fig. 6. As can be seen, both possible reaction schemes lead to an adequate simulation of the experimental spectrum, but the agreement is slightly better when the hole transfer is assumed to be the first step. Thus, the polarization pattern is consistent with either of the two possible reaction schemes provided that the sign of the exchange coupling is the same for both of them.

## 4 Conclusions

The TREPR data allow the following conclusions to be made: (1) light-induced charge separation generating the state $(BDP\text{-}TPA_2)^{+\cdot}\text{-}(C_{60})^{\bullet-}$ occurs in the triad following excitation of $AlPorF_3$. (2) The lifetime of the $(BDP\text{-}TPA_2)^{\bullet+}\text{-}(C_{60})^{\bullet-}$ state is ~ 90 ns. (3) The charge separation occurs via an intermediate radical pair state that has a lifetime on the order of a few nanoseconds, showing that the triad supports multistep sequential electron transfer. However, which of the two possible intermediates is formed remains ambiguous. Their calculated energies show that the driving force for electron transfer from $^1$AlPor* to $C_{60}$ is greater than for hole transfer from $^1$AlPor* to $BDP\text{-}TPA_2$. However, the relative rates of the two reactions also depend on the electronic coupling and the reorganization energy, $\lambda$. Geometry optimizations of the porphyrin radical cation and radical anion show that the minimum energy geometry of $(AlPorF_3)^{\bullet-}$ is substantially different from that of the neutral molecule and $(AlPorF_3)^{\bullet+}$. The root means square difference between the neutral porphyrin and radical anion structures was computed to be 1.347 Å, while for the radical cation it is only 0.401 Å. In addition, the reorganization energy for reduction of $C_{60}$ is known to be very small [46] and is probably smaller than that for oxidation of $(BDP\text{-}TPA_2)^{\bullet+}$, which has greater structural flexibility. This suggests that there is a significant difference in the reorganization energies for the two possible initial charge transfer steps, with a larger value of $\lambda$ for the hole transfer from $^1$AlPor* to $BDP\text{-}TPA_2$. Given the fairly large driving force of at least − 450 meV for the two reactions, the larger reorganization energy most likely results in a lower activation energy. The bridge between $BDP\text{-}TPA_2$ and AlPor is also shorter than that between $AlPorF_3$ and $C_{60}$, which probably results in stronger electronic coupling. Thus, the properties of the complex point to a faster rate for hole transfer to $BDP\text{-}TPA_2$ compared to electron transfer to $C_{60}$, which is also consistent with previously reported transient absorbance data [31].

**Acknowledgements** This work was supported by a Discovery Grant from the Natural Sciences and Engineering Research Council, Canada, (Grant 2015-04021 to AvdE), the US National Science Foundation (Grant no. 2000988 to FD) and startup grants from the University of Minnesota Duluth to PPK. PPK would like to thank SES Research for $C_{60}$ material grant.

## References

1. J. Deisenhofer, J.R. Norris, *Photosynthetic Reaction Center* (Academic Press, Cambridge, 2013)
2. S. Fukuzumi, Y.-M. Lee, W. Nam, Biochem. Soc. Trans. **46**, 1279 (2018)
3. S.J. Mora, E. Odella, G.F. Moore, D. Gust, T.A. Moore, A.L. Moore, Acc. Chem. Res. **51**, 445 (2018)
4. J. Barber, P.D. Tran, J.R. Soc, Interface **10**, 20120984 (2013)
5. A.C. Benniston, A. Harriman, Mater. Today **11**, 26 (2008)

6. S. Berardi, S. Drouet, L. Francàs, C. Gimbert-Suriñach, M. Guttentag, C. Richmond, T. Stoll, A. Llobet, Chem. Soc. Rev. **43**, 7501 (2014)
7. D. Gust, T.A. Moore, A.L. Moore, Acc. Chem. Res. **42**, 1890 (2009)
8. H. Imahori, Y. Mori, Y. Matano, J. Photochem. Photobiol. C Photochem. Rev. **4**, 51 (2003)
9. I. McConnell, G. Li, G.W. Brudvig, Chem. Biol. **17**, 434 (2010)
10. C.D. Buckley, D.A. Hunter, P.J. Hore, K.A. McLauchlan, Chem. Phys. Lett. **135**, 307 (1987)
11. P.J. Hore, D.A. Hunter, C.D. McKie, A.J. Hoff, Chem. Phys. Lett. **137**, 495 (1987)
12. Y.E. Kandrashkin, K.M. Salikhov, A. van der Est, D. Stehlik, Appl. Magn. Reson. **15**, 417 (1998)
13. K.M. Salikhov, Y.E. Kandrashkin, A.K. Salikhov, Appl. Magn. Reson. **3**, 199 (1992)
14. Y.E. Kandrashkin, K.M. Salikhov, D. Stehlik, Appl. Magn. Reson. **12**, 141 (1997)
15. C.R. Timmel, C.E. Fursman, A.J. Hoff, P.J. Hore, Chem. Phys. **226**, 271 (1998)
16. T. Biskup, Mol. Phys. **111**, 3698 (2013)
17. A. van der Est and P. K. Poddutoori, in *Photosynth. Struct. Mech. Appl.*, edited by H. J. M. Hou, M. M. Najafpour, G. F. Moore, and S. Allakhverdiev I. (Springer, 2017), pp. 359–387
18. A. van der Est, Biochim. Biophys. Acta BBA-Bioenerg. **1507**, 212 (2001)
19. S. Weber, EMagRes **6**, 255 (2007)
20. C.W. Kay, M. Di Valentin, K. Möbius, J. Chem. Soc. Perkin Trans. **2**, 2563 (1997)
21. N. Zarrabi, P.K. Poddutoori, Coord. Chem. Rev. **429**, 213561 (2021)
22. S. Fukuzumi, Y.-M. Lee, W. Nam, Tetrahedron **76**, 131024 (2020)
23. P. Mondal, S.P. Rath, Coord. Chem. Rev. **405**, 213117 (2020)
24. V. Nikolaou, A. Charisiadis, C. Stangel, G. Charalambidis, A.G. Coutsolelos, C-J. Carbon Res. **5**, 57 (2019)
25. J. Otsuki, J. Mater. Chem. A **6**, 6710 (2018)
26. P.K. Poddutoori, G.N. Lim, M. Pilkington, F. D'Souza, A. van der Est, Inorg. Chem. **55**, 11383 (2016)
27. P.K. Poddutoori, N. Zarrabi, A.G. Moiseev, R. Gumbau-Brisa, S. Vassiliev, A. van der Est, Chem. Eur. J. **19**, 3148 (2013)
28. P.K. Poddutoori, G.N. Lim, A.S. Sandanayaka, P.A. Karr, O. Ito, F. D'Souza, M. Pilkington, A. van der Est, Nanoscale **7**, 12151 (2015)
29. P.K. Poddutoori, L.P. Bregles, G.N. Lim, P. Boland, R.G. Kerr, F. D'Souza, Inorg. Chem. **54**, 8482 (2015)
30. P.K. Poddutoori, A.S. Sandanayaka, N. Zarrabi, T. Hasobe, O. Ito, A. van der Est, J. Phys. Chem. A **115**, 709 (2011)
31. N. Zarrabi, C.O. Obondi, G.N. Lim, S. Seetharaman, B.G. Boe, F. D'Souza, P.K. Poddutoori, Nanoscale **10**, 20723 (2018)
32. F. Neese, Wiley Interdiscip. Rev. Comput. Mol. Sci. **2**, 73 (2012)
33. F. Neese, Wiley Interdiscip. Rev. Comput. Mol. Sci. **8**, e1327 (2018)
34. J.P. Perdew, K. Burke, M. Ernzerhof, Phys. Rev. Lett. **77**, 3865 (1996)
35. S. Grimme, S. Ehrlich, L. Goerigk, J. Comput. Chem. **32**, 1456 (2011)
36. F. Weigend, R. Ahlrichs, Phys. Chem. Chem. Phys. **7**, 3297 (2005)
37. R.A. Kendall, H.A. Früchtl, Theor. Chem. Acc. **97**, 158 (1997)
38. M.D. Hanwell, D.E. Curtis, D.C. Lonie, T. Vandermeersch, E. Zurek, G.R. Hutchison, J. Cheminformatics **4**, 17 (2012)
39. A.K. Rappé, C.J. Casewit, K.S. Colwell, W.A. Goddard III., W.M. Skiff, J. Am. Chem. Soc. **114**, 10024 (1992)
40. V. Barone, M. Cossi, J. Phys. Chem. A **102**, 1995 (1998)
41. Y. Kajii, T. Nakagawa, S. Suzuki, Y. Achiba, K. Obi, K. Shibuya, Chem. Phys. Lett. **181**, 100 (1991)
42. Y.E. Kandrashkin, A. van der Est, Appl. Magn. Reson. **31**, 105 (2007)
43. Y. Kandrashkin, A. van der Est, Spectrochim. Acta. A. Mol. Biomol Spectrosc. **57**, 1697 (2001)
44. S. Stob, J. Kemmink, R. Kaptein, J. Am. Chem. Soc. **111**, 7036 (1989)
45. I.V. Zhukov, A.S. Kiryutin, M.S. Panov, N.N. Fishman, O.B. Morozova, N.N. Lukzen, K.L. Ivanov, H.-M. Vieth, R.Z. Sagdeev, A.V. Yurkovskaya, Magn. Reson. Discuss. **2**, 1 (2021)
46. H. Imahori, N.V. Tkachenko, V. Vehmanen, K. Tamaki, H. Lemmetyinen, Y. Sakata, S. Fukuzumi, J. Phys. Chem. A **105**, 1750 (2001)